

DualPM: Dual Posed-Canonical Point Maps for 3D Shape and Pose Reconstruction

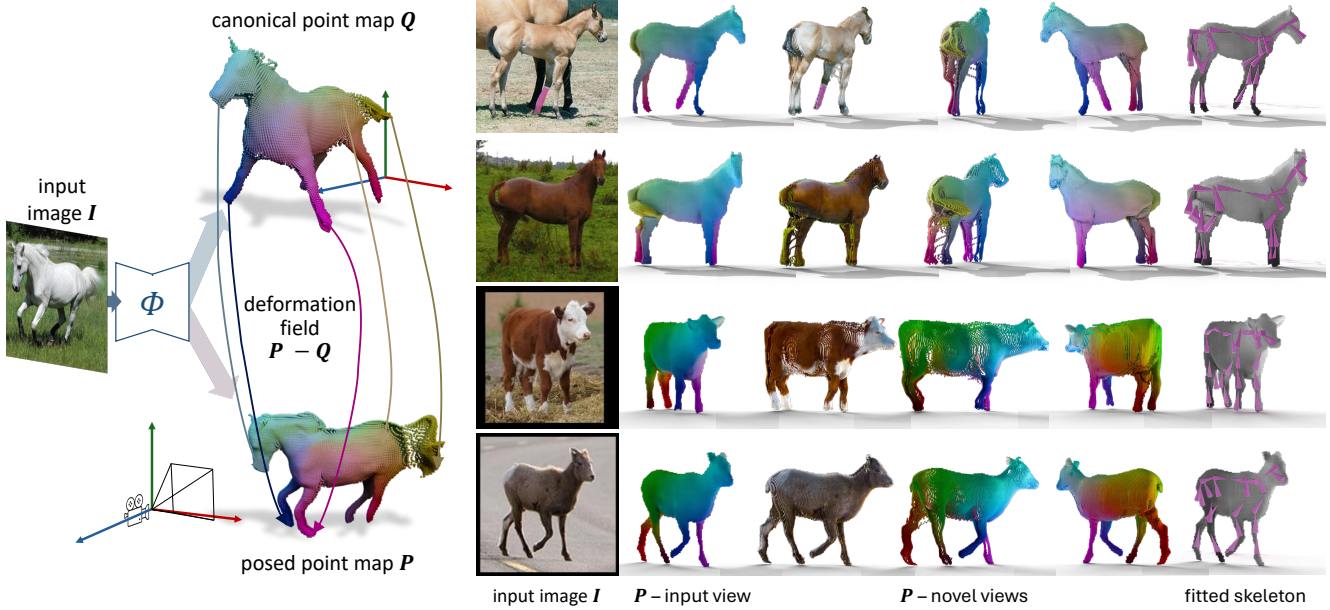
Ben Kaye^{1*}Tomas Jakab^{1*}Shangzhe Wu^{2,3}Christian Ruprecht¹Andrea Vedaldi¹¹University of Oxford²Stanford University³University of Cambridgedualpm.github.io

Figure 1. *Left:* We map an image of an object to its **Dual Point Maps** (DualPMs), a pair of point maps P , defined in a camera space, and Q , defined in a canonical space where the object has a neutral pose. The pose is thus given by the flow $P - Q$. *Right:* The DualPMs are easy to predict with a neural network, enabling effective 3D object reconstruction and facilitating geometric tasks like detecting 3D keypoints and fitting a 3D skeleton. For visualization, we color each point with its coordinate in the canonical point maps.

Abstract

The choice of data representation is a key factor in the success of deep learning in geometric tasks. For instance, DUS3R recently introduced the concept of viewpoint-invariant point maps, generalizing depth prediction and showing that all key problems in the 3D reconstruction of static scenes can be reduced to predicting such point maps. In this paper, we develop an analogous concept for a very different problem: the reconstruction of the 3D shape and pose of deformable objects. To this end, we introduce Dual Point Maps (DualPM), where a pair of point maps is extracted from the same image—one associating pixels to their

3D locations on the object and the other to a canonical version of the object in its rest pose. We also extend point maps to amodal reconstruction to recover the complete shape of the object, even through self-occlusions. We show that 3D reconstruction and 3D pose estimation can be reduced to the prediction of DualPMs. Empirically, we demonstrate that this representation is a suitable target for deep networks to predict. Specifically, we focus on modeling quadrupeds, showing that DualPMs can be trained purely on synthetic 3D data, consisting of one or two models per category, while generalizing effectively to real images. With this approach, we achieve significant improvements over previous methods for the 3D analysis and reconstruction of such objects.

*Equal contribution.

1. Introduction

An important question in 3D computer vision is finding the optimal way of interfacing visual geometry and neural networks. One approach is to use neural networks for pre-processing, for instance, to detect and match image keypoints. Once these 2D primitives are extracted, visual geometry can be used to infer the 3D structure of the scene by solving a system of equations or via optimization [63]. The alternative approach is to task the neural network with outputting *directly* the geometric quantities of interest, such as depth maps [79] or the camera pose [62].

Until recently, the general consensus was that inferring accurate 3D information should be, whenever possible, left to visual geometry, leaving to neural networks to fill gaps such as feature matching and monocular prediction. However, this view is increasingly challenged as researchers find better ways of reducing geometric tasks to the calculation of quantities that can be predicted very effectively by neural networks. Most recently, DUS3R [9, 66] has demonstrated the power of predicting *point maps*, namely images that associate each pixel with its corresponding 3D point in the scene. They show that many tasks in the reconstruction of static scenes, such as matching, camera estimation, and triangulation, can be solved trivially from the point maps predicted by a neural network.

In this work, we ask whether a similar intuition applies to a different class of problems, namely the monocular reconstruction of the *3D shape and pose of deformable objects*. We do so by developing a new network-friendly representation, which we call *Dual Point Maps* (DualPMs).

Our setting is a substantial departure from DUS3R, and so are their point maps and our DualPMs. Nevertheless, the starting point is the same: a point map in both DUS3R and DualPM associates each image pixel with its corresponding 3D point on the object. Predicting this point map gives us a 3D reconstruction of the object, which is useful but provides no information about the *pose* of the object.

To clarify this further, consider the example of a horse. Its pose is *defined* as the deformation that takes the horse from its neutral pose to the pose observed in the image. Hence, reconstructing its pose means finding the transformation, or deformation field, between two versions of the 3D object: the one seen in the image and the *canonical* version of the same object in a neutral pose. Knowledge of a single point map gives no information about this transformation. So the question is: How can we extend point maps so that recovering this deformation field becomes trivial?

To solve this problem, our DualPMs predicts not one, but *two* point maps from the *same image* (Fig. 1). They map each pixel to *two* versions of the same 3D point. The first version is the usual reconstruction of the object in 3D. The second version, however, is the *location of the point in the canonical version of the object*. With this representation, it is easy to

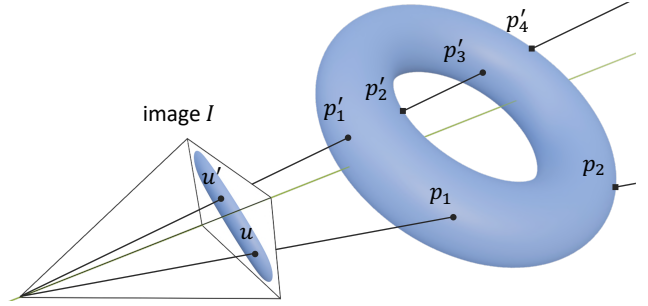


Figure 2. An *amodal point map* associates each pixel u to an even number of objects points p_i , corresponding to the locations where the pixel's ray intersects the object's surface. Predicting an amodal point map reconstructs the entire object despite self-occlusions.

recover the pose of the object: in fact, the deformation field that we wish to recover is simply the *difference* between the two point maps. Knowledge of this deformation field is, in turn, useful for various analysis tasks, such as recovering 3D keypoints or estimating the object's articulation in terms of a skeleton (see Fig. 1).

The canonical version of the point map is also *viewpoint invariant* and bears some resemblance to the Normalized Object Coordinates of [60] and the Canonical Surface Maps of [25, 57]. As such, its prediction is similar to a keypoint labeling problem, which can be solved effectively by a neural network. Furthermore, we show that the canonical point map is also a good feature map in its own right; in fact, our model predicts the posed point map from the canonical one, using it as a feature extractor instead of, for instance, DINOv2 [45].

A shortcoming of point maps, in general, is that they only reconstruct the *visible* part of the object. To address this issue, we introduce the idea of estimating *amodal* point maps; namely, each pixel is mapped not only to the visible point of the object but to *all* points on the object that project onto that pixel, regardless of self-occlusions (Fig. 2). To effectively represent such point maps for neural network prediction, we propose a layered representation. In this representation, the first layer encodes the visible points, and each subsequent layer captures the next set of points occluded by the previous layer. This concept is similar to depth peeling, a standard technique used in rasterization in computer graphics. With this extension, we can provide a full reconstruction of the object's shape and pose.

To test our ideas, we consider the problem of reconstructing the 3D shape and pose of quadrupeds from monocular images. Quadrupeds represent a widely studied category of deformable objects [18, 26, 33, 71, 72], with synthetic 3D data readily available for this class [18], enabling controlled evaluations. Furthermore, we show that synthetic data derived from one or two 3D models per category is sufficient to train a DualPM model that generalizes robustly to real-world data thanks to our effective representation, which makes

learning relatively easy. With this, we demonstrate that we can improve previous methods by a large margin for the 3D analysis and reconstruction of this type of object, even on out-of-domain real-world datasets, both in terms of correspondence and 3D reconstruction. We also show the ability of the point maps to reconstruct the pose of the object in terms of their deformation fields and suggest applications such as fitting articulated 3D skeletons to the object, which can be used for motion transfer and animations.

To summarize, our contributions are as follows:

1. We introduce the novel concept of DualPM, reducing monocular 3D shape and pose reconstruction to predicting a *pair* of point maps: one in canonical space and the other in posed camera space.
2. We extend point maps to enable amodal reconstruction with a layered representation, producing the complete 3D shape of articulated objects.
3. We demonstrate that DualPMs can be effectively predicted by neural networks, with synthetic data sufficing for training.
4. We show that tasks like 3D reconstruction, keypoint transfer, deformation estimation, and skeleton fitting reduce to predicting DualPMs.
5. We achieve significant improvements over prior methods for 3D analysis and reconstruction of quadrupeds, even when trained on minimal synthetic data.

2. Related work

Deformable reconstruction. Our work is related to the reconstruction of deforming scenes. Many such works consider the *optimization* approach, where a 4D model of the scene is fitted to a video sequence. In works like Video Pop-up [51], Monocular 3D [27], and MonoRec [67], the 3D reconstruction of different video frames is regularized, for instance, to enforce approximate local rigidity.

More often, the 4D scene is represented as the deformation of a canonical configuration. DynamicFusion [43] is an early example of this approach. More recent works like Neural Volumes [40] reconstruct both shape and appearance. D-NeRF [47], Neural Radiance Flow [8], Neural Scene Flow Fields [31], Dynamic Video Synthesis [16], DynIBaR [32], and MorpheuS [61] extend NeRF [42] with dense deformation fields to capture motion. Similarly, 4D Gaussian Splatting [68], Gaussian Flow [36], DynMF [24], GauFRe [34], MoSca [28], Street Gaussians [75], Dynamic Gaussian Marbles [56], Shape of Motion [65], Ego Gaussians [85], and 4DGS [68] also estimate deformations, but in the context of 3D Gaussian Splatting [21] rather than NeRF.

Rather than modeling dense deformation fields, approaches like Dynamic NeRF [15], Seeing 3D Objects [52], K-planes [14], and HexPlane [5] add time or pose parameterization to the NeRF model. Approaches like 4D Visualization [2] and NVSD [84] predict novel views of a dynamic

scene without explicit 3D reconstruction.

Fourier PlenOctrees [64], NeRFPlayer [54], and RT-4DGS [80] focus on the problem of storing and rendering 4D models efficiently. 4DGen [83], Align Your Gaussians [37], DreamScene4D [7], and L4GM [48] consider the problem of generating 4D models from text (text-to-4D). PhysGaussian [74], MD-Splatting [10], Gaussian Splashing [13], and VR-GS [19] consider reconstruction and generation of 4D scenes that account for physical principles.

Works like Neural Human Video Rendering [39], AutoAvatar [1], Neural Body [46], Dynamic Facial RF [53], Relighting4D [6], Animate124 [88], Dynamic Gaussian Mesh [38], and IM4D [35] specialize in the reconstruction of articulated characters like humans and animals. Often, these define the object in a canonical neutral pose and encode the pose as a deformation thereof.

Learning deformable 3D object categories. Works like 3D Menagerie [89], Unsupervised 3D [69], LASR [76], BANMo [77], Dessie [29], DOVE [71], LASSIE [81], MagicPony [70], Farm3D [18], 3D-Fauna [33], and others [17, 50, 78, 82, 90] have considered the problem of learning models of 3D object categories. In these models, the pose is expressed as the object deformation with respect to a version of the object in a neutral pose, which usually takes the form of a category-level template. Such a template can be learned either in a weakly-supervised manner [18, 33, 70, 71, 78, 81, 82] or from 3D data, most notably SMPL [41], SMAL [3], and more recently, VAREN [91]. Concurrent Dessie also introduces a synthetic data generation pipeline similar to ours.

Point maps and canonical maps. DUSt3R [66] was the first paper to intuit the power of predicting point maps instead of depth for 3D reconstruction. The follow-up MASt3R [9] builds on this to obtain a state-of-the-art Structure-from-Motion (SfM) system. MonST3R [87] extends DUSt3R to monocular video, reconstructing dynamic point maps in a fixed reference frame.

The concept of learning a map that sends pixels to canonical object points can be found in the dense equivariant mapping of [57–59]. Normalized Object Coordinates (NOCs) [60] modify this idea for rigid objects by sending pixels to 3D points defined on the object’s surface in a canonical pose. Our approach also does this but with two key differences: (1) the input object is deformable rather than rigid, and (2) we predict dual point maps, which encode the object deformation beyond a simple rigid transformation.

3. Method

Let $I \in \mathbb{R}^{3 \times H \times W}$ be an image containing a deformable object we wish to reconstruct in 3D, along with its pose. We assume that a mask $M \in \{0, 1\}^{H \times W}$ is available, indicating the object’s location in the image. Next, we introduce

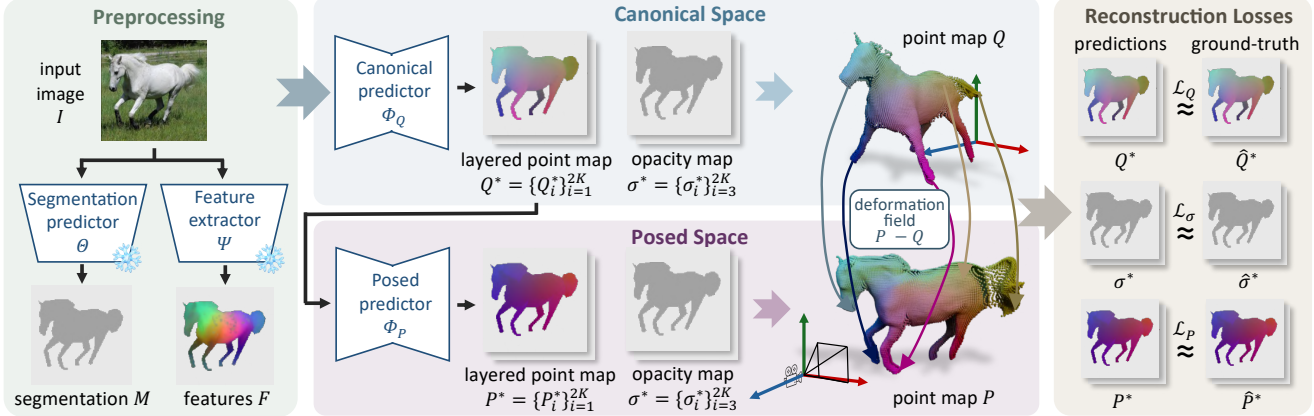


Figure 3. **Method overview.** We preprocess the input image I by obtaining a segmentation mask M and image features F using pretrained networks. Subsequently, we predict the layered canonical point map $\{Q_i^*\}_{i=1}^{2K}$. Conditioned on $\{Q_i^*\}_{i=1}^{2K}$, we predict the layered posed point map $\{P_i^*\}_{i=1}^{2K}$, along with the associated opacity maps $\{\sigma_i^*\}_{i=1}^{2K}$. Both layered point maps are then decoded to produce the canonical point map Q and the posed point map P . The training process is supervised using the ground truth point maps and opacity maps.

the concept of *dual point maps* (Sec. 3.1) and its *amodal* extension (Sec. 3.2).

3.1. Dual point maps

A *point map* $P \in \mathbb{R}^{3 \times H \times W}$ is a tensor containing a 3D point for each pixel of the input image I . We are particularly interested in the pixels $\mathbf{u} \in M$ contained within the object’s mask M . Here, \mathbf{u} is the image of some point \mathbf{p} that belongs to the surface of the object, known as the *imaged point*. The image sample $I(\mathbf{u})$ is the color of the imaged point (an RGB triplet), and $\mathbf{p} = P(\mathbf{u}) \in \mathbb{R}^3$ is the 3D location of the point, expressed in the reference frame of the camera.

By estimating the point map P from the image I , we reconstruct the visible portion of the 3D object. This is similar to predicting a depth map but provides strictly *more* information. In fact, the 3D point *does not* depend on the camera’s intrinsic parameters, such as the focal length, as it is directly expressed in the camera’s reference frame. As shown in [66], this fact can be used to *infer* the camera intrinsics. However, this point map does not capture the object’s deformation and thus cannot be used by itself to recover its articulated pose.

We address this limitation by introducing the novel concept of *Dual Point Maps* (DualPMs). In addition to P , we predict a second point map $Q \in \mathbb{R}^{3 \times H \times W}$ defined in *canonical space*. By “canonical”, we mean two things: first, the points in Q are expressed in the object reference frame rather than in the camera frame; second, the object is in a canonical pose, usually a neutral pose. Hence, unlike P , the point map Q is invariant to the object’s pose and deformation.

The pair of point maps P and Q implicitly encode the object deformation: they tell us that pixel \mathbf{u} corresponds to a point that is located at $\mathbf{q} = Q(\mathbf{u})$ in the rest pose and at $\mathbf{p} = P(\mathbf{u})$ once posed. This provides rich information about the object’s pose. For example, given two images I_1 and I_2

of the object in two different poses, we can match a pixel \mathbf{u}_1 in the first image to its corresponding pixel \mathbf{u}_2 in the second by matching the corresponding canonical points $Q_1(\mathbf{u}_1)$ and $Q_2(\mathbf{u}_2)$, *i.e.*,

$$\mathbf{u}_2(\mathbf{u}_1) = \underset{\mathbf{u}_2 \in M_2}{\operatorname{argmin}} \|Q_1(\mathbf{u}_1) - Q_2(\mathbf{u}_2)\|^2.$$

This works because the canonical points are view- and pose-invariant. Then, we can infer the so-called ‘scene flow’, or motion between the 3D points, as $P_2(\mathbf{u}_2(\mathbf{u}_1)) - P_1(\mathbf{u}_1)$.

Predicting the dual point maps. To predict the dual point maps from the image I , we introduce a predictor neural network $(P, Q) = \Phi(I)$. Its architecture is illustrated in Fig. 3. A key property of the canonical point map Q is its *invariance* to the object’s pose and deformation. This invariance simplifies its prediction by a neural network, as it reduces the task to a pixel labeling problem. To further ease the prediction of Q and improve generalization, we leverage recent advances in self-supervised image feature learning [11, 45, 86], and condition its prediction on strong features F extracted from the image I using a pre-trained network Ψ , $F = \Psi(I)$ from [86]. These features serve as a good proxy for the canonical point map, as they have been shown to be nearly invariant to the object’s pose and deformation, thereby simplifying the network’s task. We then condition the prediction of P on Q instead of F , as this improves the model’s generalization on out-of-distribution images, as demonstrated in Sec. 4.4. This shows that learning canonical point maps as an intermediate representation benefits the 3D reconstruction task. To summarize, we first predict Q using the features F , and then condition the prediction of P on Q :

$$Q = \Phi_Q(\Psi(I)), \quad P = \Phi_P(Q).$$

We extend both networks Φ_Q and Φ_P to also predict a

per-pixel confidence score. For example, the map Φ_P outputs the map $c_P(\mathbf{u}) > 0$, which is used to train the model using the self-calibrated L2 loss from [20, 44, 66]:

$$\mathcal{L}_P = \frac{1}{|M|} \sum_{\mathbf{u} \in M} c_P(\mathbf{u}) \|\hat{P}(\mathbf{u}) - P(\mathbf{u})\|^2 - \alpha \log c_P(\mathbf{u}),$$

where $\alpha > 0$ is a constant and \hat{P} is the ground-truth point map. An analogous loss \mathcal{L}_Q is used for Φ_Q .

3.2. Amodal point maps

A limitation of dual point maps is that they only capture the visible portion of the object. We now show how to predict a complete 3D point cloud for the object, including points that are not visible due to *self-occlusion*.

To this end, we introduce the concept of an *amodal point map*. Namely, we associate each pixel $\mathbf{u} \in M$ within the object mask to the sequence of 3D points $(\mathbf{p}_1, \mathbf{p}_2, \dots)$ that intersect the camera ray through \mathbf{u} in order of increasing distance from the camera center. Hence, $\mathbf{p} = \mathbf{p}_1$ is the imaged point considered in Sec. 3.1, \mathbf{p}_2 is the point that would be imaged if a hole were plucked in the object surface at \mathbf{p}_1 , and so on. The goal is to predict the *amodal point map* \mathcal{P} , defined as the map that associates each pixel \mathbf{u} with the sequence of 3D points $\mathcal{P}(\mathbf{u}) = (\mathbf{p}_1, \mathbf{p}_2, \dots)$.

The length of the sequence $\mathcal{P}(\mathbf{u})$ is not fixed but depends on the pixel \mathbf{u} . The sequence length is always even because the ray must exit the object once it enters it, as we assume the camera is positioned outside the object. To account for this, we extend the network Φ_P to first predict a pair of points $(\mathbf{p}_1, \mathbf{p}_2)_1$ for each pixel \mathbf{u} . Subsequently, additional sets of outputs $(\mathbf{p}_{2k-1}, \mathbf{p}_{2k})_k$ are added for $k \in [2, K]$, where K denotes the total number of pairs, capturing further potential ray intersections with the object. Unlike the first set of intersections, these additional intersections may not always occur; therefore, we also predict opacities $(\sigma_{2k-1}, \sigma_k)_k$ for these cases. As a result, each pixel \mathbf{u} is mapped to $3 \times 2 + (3 + 1) \times 2 \times (K - 1)$ scalar outputs. The network Φ_Q is extended similarly. The losses \mathcal{L}_P and \mathcal{L}_Q are also extended to account for the amodal point maps. Additionally, we add a loss \mathcal{L}_σ to supervise the opacity predictions.

Layered point maps. To efficiently represent the amodal point map for neural network prediction, we introduce an image-based *layered* representation for DualPMs, denoted as (P^*, Q^*) . In this representation, the first layer encodes the visible points, and each consecutive layer captures the next set of points occluded by the previous layer. We also represent the opacity maps σ^* in the same layered fashion.

Since we supervise our method with synthetic data, we can easily generate training targets for this representation. Each vertex of the object mesh is assigned a 6D attribute, consisting of the posed vertex’s 3D position and the corresponding vertex’s 3D position in canonical space. The



Figure 4. **Synthetic training data.** We generate synthetic training data by rendering a rigged 3D model of a category in various poses with different environmental maps and under random viewpoints.

mesh is then rendered from the camera’s viewpoint. During the rendering process, the rasterizer generates a set of pixel-aligned layers, $L_i \in \mathbb{R}^{6 \times H \times W}$, which contain the rendered 6D attributes, together with the associated opacity map $\hat{\sigma}_i^* \in [0, 1]^{H \times W}$ for every ray-object intersection. We iterate through the rasterized layers from the front to the back until the number of layers specified for our model is reached. This approach yields ground-truth DualPMs with a number of layers corresponding to the ray-object intersections. We split the attributes of each layer corresponding to the canonical and posed positions, yielding ground-truth layered canonical point maps

$$\hat{Q}^* = (\hat{Q}_1^*, \hat{Q}_2^*, \dots, \hat{Q}_N^*), \quad \hat{Q}_i^* \in \mathbb{R}^{3 \times H \times W},$$

and layered posed point maps

$$\hat{P}^* = (\hat{P}_1^*, \hat{P}_2^*, \dots, \hat{P}_N^*), \quad \hat{P}_i^* \in \mathbb{R}^{3 \times H \times W},$$

with their associated opacity maps σ_i^* . The number of layers N corresponds to $2K$. The canonical Q and posed P point maps can then be extracted from this representation by masking out transparent points.

3.3. Training

We train a separate model for each category using synthetic data generated from one or two articulated 3D assets per category sourced from the Animodel dataset [18]. We use a separate model for each biological sex in cases where animals exhibit distinct anatomical structures specific to males and females, such as horns in cattle. Following the data generation pipeline described in Animodel, we randomly sample object poses, camera poses, and illumination conditions. These are modeled by randomly sampling from a collection of environment maps. For each sample, we render the object into an image I and generate the corresponding image-based layered paired point maps P^* and Q^* , which serve as targets for the model, using the procedure detailed in Sec. 3.2. We illustrate our synthetic training data in Fig. 4.

4. Experiments

We evaluate our DualPM in terms of both qualitative (Sec. 4.1) and quantitative performance (Sec. 4.2) across

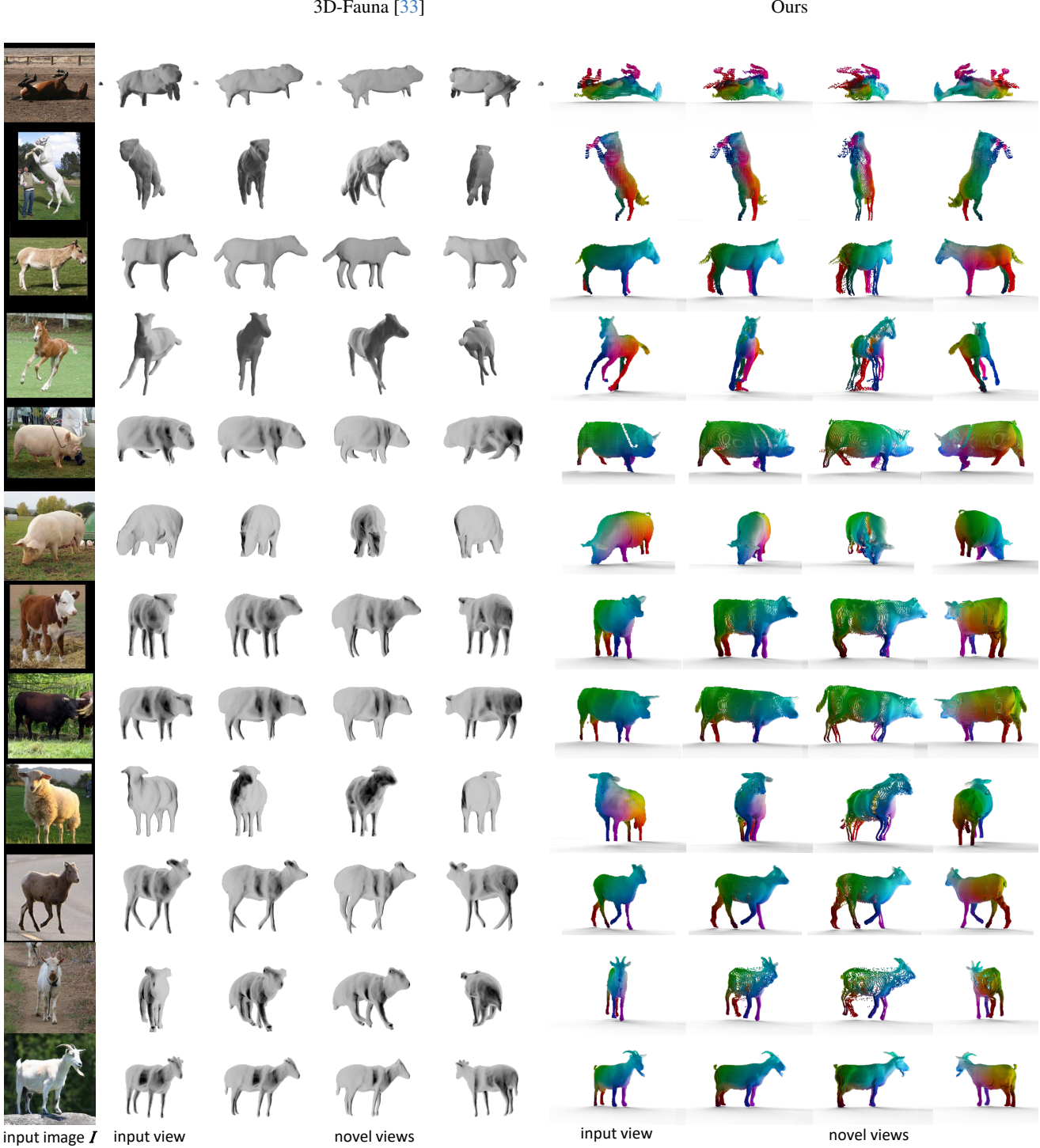


Figure 5. **Comparison with the state-of-the-art.** We compare our method with 3D-Fauna [33]. For visualization, we paint each point of the recovered point map P with its canonical coordinate. Our reconstructed shape aligns more closely with the object’s structure compared to 3D-Fauna and adapts well to large variations within the object category. Our method reliably recovers shapes outside its training distribution, such as foals and donkeys (rows 3 and 4). It also performs well on very challenging poses (rows 1 and 2), where 3D-Fauna completely fails.

several quadruped categories. We demonstrate that our DuAlPM can be used to fit 3D skeletons for motion transfer and

animations (Sec. 4.3), assess the impact of our design choices in an ablation study (Sec. 4.4), and showcase zero-shot gen-

Method	PCK (%)			RMS Chamfer Distance (cm)			Model-view RMS Chamfer Distance (cm)		
	Horse	Cow	Sheep	Horse	Cow	Sheep	Horse	Cow	Sheep
A-CSM [26]	32.9	26.3	28.6	11.75 \pm 3.83	9.52 \pm 2.41	9.24 \pm 2.40	38.13 \pm 13.89	33.51 \pm 11.52	29.04 \pm 9.35
MagicPony [72]	42.9	42.5	41.2	11.19 \pm 3.08	10.29 \pm 2.08	—	20.82 \pm 13.04	25.39 \pm 13.43	—
Farm3D [18]	49.1	40.2	36.1	11.34 \pm 3.22	9.63 \pm 2.02	11.01 \pm 1.87	29.52 \pm 15.73	21.34 \pm 12.85	21.52 \pm 9.84
3D-Fauna [33]	53.9	—	—	11.86 \pm 3.03	10.54 \pm 2.26	9.61 \pm 2.15	15.70 \pm 6.82	14.08 \pm 4.20	12.24 \pm 3.17
Trellis [73]	—	—	—	6.93 \pm 4.13	6.80 \pm 3.24	5.91 \pm 2.93	36.82 \pm 16.02	26.54 \pm 13.14	26.56 \pm 12.06
DualPM (Ours)	73.2	66.86	66.82	4.30 \pm 1.50	3.18 \pm 1.06	3.30 \pm 1.20	5.49 \pm 1.75	4.03 \pm 2.11	4.22 \pm 2.18

Table 1. **Quantitative evaluation.** We evaluate on PASCAL VOC, reporting PCK@0.1 (higher is better \uparrow), and on Animodel-Points, a derivative of Animodel [18] for evaluating point clouds, reporting the Root-mean-square-error of bi-directional Chamfer Distance in centimeters (lower is better \downarrow). Point clouds are registered using the iterative closest points algorithm with bidirectional chamfer distance as its cost function. We report both the results with and without rotation alignment. Our model, trained solely on data from one or two models per category, outperforms other state-of-the-art approaches, and has superior camera alignment.

eralization to unseen quadruped categories. Additionally, we discuss the limitations of our method and provide technical and implementation details in the supplementary material.

4.1. Qualitative evaluation

We qualitatively evaluate our method on challenging in-the-wild images of quadrupeds, specifically the horse, cow, sheep, and pig categories from the PASCAL VOC dataset [12] and goat images from [4]. The results are presented in Figs. 1 and 5. Our method successfully recovers the 3D shape and pose of quadrupeds from a single image, despite significant variations in pose, shape, and appearance within each animal category. For instance, in the horse category, although the method is trained on a single adult horse model, it generalizes well to foals and dwarf horses. We also compare our method with the state-of-the-art approach for single-view reconstruction of deformable objects, 3D-Fauna [33], and present side-by-side comparisons in Fig. 5. Our method performs better in recovering the shape and pose than 3D-Fauna, which struggles to accurately follow the object’s structure and fails to reconstruct intricate details specific to each object.

4.2. Quantitative evaluation

Following prior work on deformable object reconstruction [26, 30, 33, 72], we evaluate our method on the key-point transfer task using the PASCAL VOC dataset [12]. We adhere to the protocol of [26] and report the percentage of correctly transferred keypoints with a 10% threshold (PCK@0.1) between pairs of images. The results are presented in Tab. 1, where we compare our method with state-of-the-art approaches.

We also measure the bi-directional Chamfer distance between the predicted point maps and the ground truth 3D shape on the Animodel dataset introduced in Farm3D [18]. This dataset comprises renderings of 3D models of horses, cows, and sheep in various poses. To ensure a fair comparison, we train a separate model on data that excludes the poses

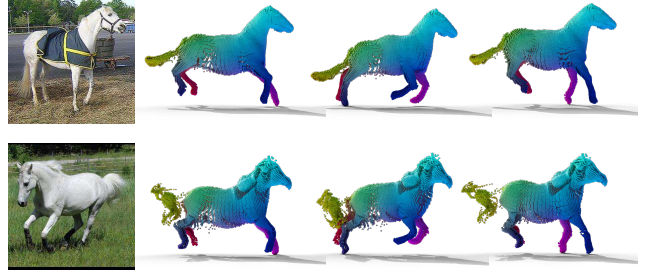


Figure 6. **Animation.** DualPMs allow for fitting a 3D skeleton, which can subsequently be used to animate the 3D reconstruction by utilizing existing animations through motion retargeting.

used in this benchmark. The performance of our method and others is reported in Tab. 1¹

Our method consistently outperforms all other approaches, including self-supervised methods trained on large datasets of real images of quadruped categories (3D-Fauna [33]) and approaches trained on large-scale 3D asset datasets (Trellis [73]), demonstrating its ability to generalize to unseen poses and shapes. Moreover, it exhibits generalization to real-world images of the same category, despite being trained solely on synthetic data obtained from one or two templates per category. Additionally, it demonstrates some zero-shot generalization across categories, as shown in the supplementary material.

4.3. Skeleton fitting and animation

With a predicted DualPM (P, Q) , we can easily fit an instance-specific 3D skeleton. Our method is trained on synthetic data from a model rigged with a skeleton composed of bones B that deform the mesh. These bones are defined in

¹Amendment: the Animodel evaluation was not suitable for evaluating point clouds, and we have updated our table with an improved benchmark. The original published table is available in the appendix in Tab. A4. Benchmark details are available in App. D.

the canonical space, and each bone is associated with a set of vertices on the mesh through skinning weights.

For each point (p_i, q_i) of the DualPM (P, Q) , we identify the closest vertex of the mesh in the canonical space to the canonical point q_i , then associate the point (p_i, q_i) with the skinning weights of that vertex. For each bone $b \in B$, we identify subsets $\{(p_i, q_i)_b\}$, where the associated skinning weights between the bone b and the points (p_i, q_i) are higher than 0.5. We then compute the transformation that aligns the subset of canonical points $\{(q_i)_b\}$ to the subset of posed points $\{(p_i)_b\}$ using the Procrustes algorithm. This transformation is applied to the bone b in the canonical space to derive its corresponding pose in the posed space. This process is repeated for all bones in the skeleton to fit the 3D skeleton to the posed points. We show examples of our fitted skeletons in Fig. 1.

The fitted skeleton can then be used to animate our 3D reconstructions through motion retargeting from existing animations defined on the rigged model used for training. We demonstrate examples of this in Fig. 6.

4.4. Ablation study

We conduct an ablation study to evaluate the impact of different components of our model on its performance and report the results in Sec. 4.4. Specifically, we examine the advantages of predicting pixel-aligned point maps over directly predicting bone rotations, which are typically used to articulate a rigged mesh model in prior approaches [18, 33, 72]. To test this, we train a version of the method proposed in [33, 72] on our synthetic dataset, where the bone rotation regressor is supervised directly with ground-truth rotations.

The results show that this model performs worse than our proposed approach. We hypothesize that this disparity arises because our representation is more amenable to neural networks. Predicting pixel-aligned point maps effectively transforms the task into a pixel-labeling problem, which is simpler for neural networks to learn. In contrast, directly predicting a chain of 3D rotations for a rigged model is inherently more complex.

Additionally, we investigate the effect of conditioning the predictions of the posed point maps P on the input image features F and the canonical point maps Q . When the model is conditioned on the image features F , it tends to overfit to the more variable features of the training dataset. In contrast, conditioning the posed point maps P solely on the canonical point maps Q leads to better generalization, particularly on out-of-distribution images, as we also demonstrate qualitatively in Fig. 7.

Finally, we analyze the impact of varying the number of layers used in the layered amodal point map predictions. The performance on the Animodel benchmark shows minimal change, as self-occlusions beyond four occluded surfaces are less frequent in the dataset. The number of predicted layers

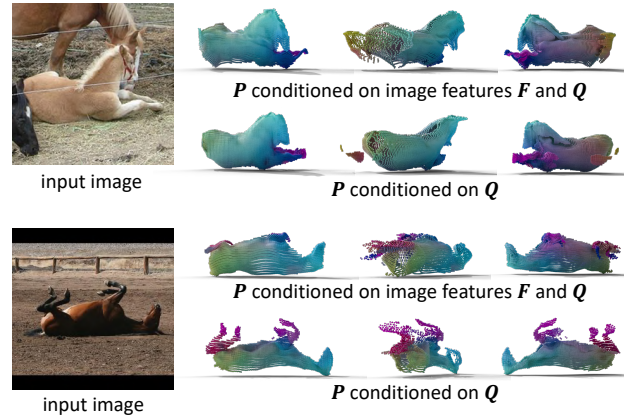


Figure 7. **Effect of different conditioning schemes.** Conditioning solely on the canonical point maps Q , as opposed to using both the image features F and the canonical point maps Q , results in better generalization, particularly in extreme out-of-distribution images.

can be easily adjusted to match the complexity of the data.

Method	RMS Chamfer Distance (cm) \downarrow
Predicting bone rotations (supervised 3D-Fauna [33])	6.79 ± 2.47
<i>Our method</i>	
8-layers	4.45 ± 1.61
4-layers	4.30 ± 1.50
<i>Ablations on 4-layer model</i>	
P conditioned on F and Q	4.54 ± 1.60
P conditioned on F	4.48 ± 1.46

Table 2. **Ablation study on Animodel-points horses category.** We report the root-mean-square bi-directional Chamfer Distance in centimetres (lower is better \downarrow) for the horse category of Animodel-points. The evaluation follows the protocol as Tab. 1.

5. Conclusion

We presented DualPMs, a novel representation for monocular 3D shape and pose reconstruction of deformable objects. Predicting DualPMs is straightforward for a neural network, and they enable solving a variety of geometric tasks for deformable objects, including not only 3D shape and pose reconstruction but also 3D keypoint localization, skeleton fitting, and motion transfer. Despite being trained solely on synthetic data generated from one or two models per category, our method generalizes effectively to real images and outperforms state-of-the-art methods on the task of 3D shape and pose reconstruction of horses, cows, and sheep.

Acknowledgments. We thank Paul Engstler for helpful discussions. Ben Kaye is supported by the EPSRC Centre for

Doctoral Training in Autonomous Intelligent Machines and Systems, EP/S024050/1. Tomas Jakab and Andrea Vedaldi are supported by ERC-CoG UNION 101001212. Tomas Jakab is also supported by VisualAI EP/T028572/1.

References

- [1] Ziqian Bai, Timur Bagautdinov, Javier Romero, Michael Zollhöfer, Ping Tan, and Shunsuke Saito. AutoAvatar: Autoregressive neural fields for dynamic avatar modeling. In *Proc. ECCV*, 2022.
- [2] Aayush Bansal, Minh Vo, Yaser Sheikh, Deva Ramanan, and Srinivasa G. Narasimhan. 4D visualization of dynamic events from unconstrained multi-view videos. In *Proc. CVPR*, 2020.
- [3] Benjamin Biggs, Thomas Roddick, Andrew W. Fitzgibbon, and Roberto Cipolla. Creatures great and SMAL: recovering the shape and motion of animals from video. In *Proc. ECCV*, 2018.
- [4] Masum Billah, Yu Jiantao, and Yu Jiang. Goat image dataset. Mendeley Data, V2, 2020.
- [5] Ang Cao and Justin Johnson. Hexplane: A fast representation for dynamic scenes. *arXiv.cs*, abs/2301.09632, 2023.
- [6] Zhaoxi Chen and Ziwei Liu. Relighting4D: Neural relightable human from videos. In *Proc. ECCV*, 2022.
- [7] Wen-Hsuan Chu, Lei Ke, and Katerina Fragkiadaki. Dream-Scene4D: dynamic multi-object scene generation from monocular videos. *arXiv*, 2405.02280, 2024.
- [8] Yilun Du, Yinan Zhang, Hong-Xing Yu, Joshua B. Tenenbaum, and Jiajun Wu. Neural radiance flow for 4d view synthesis and video processing. In *Proc. ICCV*, 2021.
- [9] Bardienus Duisterhof, Lojze Zust, Philippe Weinzaepfel, Vincent Leroy, Yohann Cabon, and Jerome Revaud. MASt3R-SfM: a fully-integrated solution for unconstrained structure-from-motion. *arXiv*, 2409.19152, 2024.
- [10] Bardienus P. Duisterhof, Zhao Mandi, Yunchao Yao, Jia-Wei Liu, Mike Zheng Shou, Shuran Song, and Jeffrey Ichnowski. MD-Splatting: Learning metric deformation from 4d gaussians in highly deformable scenes. *arXiv.cs*, 2312.00583, 2023.
- [11] Patrick Esser, Robin Rombach, and Björn Ommer. Taming transformers for high-resolution image synthesis. In *Proc. CVPR*, 2021.
- [12] M. Everingham, L. Van Gool, C. K. I. Williams, J. Winn, and A. Zisserman. The pascal visual object classes (voc) challenge. *IJCV*, 88(2):303–338, 2010.
- [13] Yutao Feng, Xiang Feng, Yintong Shang, Ying Jiang, Chang Yu, Zeshun Zong, Tianjia Shao, Hongzhi Wu, Kun Zhou, Chenfanfu Jiang, and Yin Yang. Gaussian splashing: Dynamic fluid synthesis with gaussian splatting. *arXiv.cs*, 2401.15318, 2024.
- [14] Sara Fridovich-Keil, Giacomo Meanti, Frederik Warburg, Benjamin Recht, and Angjoo Kanazawa. K-planes: Explicit radiance fields in space, time, and appearance. *arXiv.cs*, abs/2301.10241, 2023.
- [15] Guy Gafni, Justus Thies, Michael Zollhöfer, and Matthias Nießner. Dynamic neural radiance fields for monocular 4d facial avatar reconstruction. In *Proc. CVPR*, 2021.
- [16] Chen Gao, Ayush Saraf, Johannes Kopf, and Jia-Bin Huang. Dynamic view synthesis from dynamic monocular video. In *Proc. ICCV*, 2021.
- [17] Shubham Goel, Angjoo Kanazawa, and Jitendra Malik. Shape and viewpoints without keypoints. In *Proc. ECCV*, 2020.
- [18] Tomas Jakab, Ruining Li, Shangzhe Wu, Christian Rupprecht, and Andrea Vedaldi. Farm3D: Learning articulated 3D animals by distilling 2D diffusion. In *Proc. 3DV*, 2024.
- [19] Ying Jiang, Chang Yu, Tianyi Xie, Xuan Li, Yutao Feng, Huamin Wang, Minchen Li, Henry Lau, Feng Gao, Yin Yang, and Chenfanfu Jiang. VR-GS: A physical dynamics-aware interactive gaussian splatting system in virtual reality. *arXiv*, 2401.16663, 2024.
- [20] Alex Kendall and Yarin Gal. What uncertainties do we need in Bayesian deep learning for computer vision? *Proc. NeurIPS*, 2017.
- [21] Bernhard Kerbl, Georgios Kopanas, Thomas Leimkühler, and George Drettakis. 3D Gaussian Splatting for real-time radiance field rendering. *Proc. SIGGRAPH*, 42(4), 2023.
- [22] Diederik P. Kingma and Jimmy Ba. Adam: A method for stochastic optimization. *Proc. ICLR*, 2015.
- [23] Alexander Kirillov, Eric Mintun, Nikhila Ravi, Hanzi Mao, Chloe Rolland, Laura Gustafson, Tete Xiao, Spencer Whitehead, Alexander C. Berg, Wan-Yen Lo, Piotr Dollár, and Ross Girshick. Segment anything. In *Proc. CVPR*, 2023.
- [24] Agelos Kratimenos, Jiahui Lei, and Kostas Daniilidis. DynMF: Neural motion factorization for real-time dynamic view synthesis with 3D Gaussian splatting. *arXiv.cs*, abs/2312.00112, 2023.
- [25] Nilesh Kulkarni, Abhinav Gupta, and Shubham Tulsiani. Canonical surface mapping via geometric cycle consistency. In *Proc. ICCV*, 2019.
- [26] Nilesh Kulkarni, Abhinav Gupta, David F. Fouhey, and Shubham Tulsiani. Articulation-aware canonical surface mapping. In *Proc. CVPR*, pages 449–458, 2020.
- [27] Suryansh Kumar, Yuchao Dai, and Hongdong Li. Monocular dense 3D reconstruction of a complex dynamic scene from two perspective frames. In *Proc. ICCV*, 2017.
- [28] Jiahui Lei, Yijia Weng, Adam Harley, Leonidas Guibas, and Kostas Daniilidis. MoSca: dynamic gaussian fusion from casual videos via 4d motion scaffolds. *arXiv*, 2405.17421, 2024.
- [29] Ci Li, Yi Yang, Zehang Weng, Elin Hernlund, Silvia Zuffi, and Hedvig Kjellström. Dessie: Disentanglement for articulated 3D horse shape and pose estimation from images. *arXiv*, 2410.03438, 2024.
- [30] Xuetong Li, Sifei Liu, Kihwan Kim, Shalini De Mello, Varun Jampani, Ming-Hsuan Yang, and Jan Kautz. Self-supervised single-view 3D reconstruction via semantic consistency. In *Proc. ECCV*, 2020.
- [31] Zhengqi Li, Simon Niklaus, Noah Snavely, and Oliver Wang. Neural scene flow fields for space-time view synthesis of dynamic scenes. In *Proc. CVPR*, 2021.
- [32] Zhengqi Li, Qianqian Wang, Forrester Cole, Richard Tucker, and Noah Snavely. DynIBaR: Neural dynamic image-based rendering. In *Proc. CVPR*, 2023.

[33] Zizhang Li, Dor Litvak, Ruining Li, Yunzhi Zhang, Tomas Jakab, Christian Rupprecht, Shangzhe Wu, Andrea Vedaldi, and Jiajun Wu. Learning the 3D fauna of the Web. In *Proc. CVPR*, 2024.

[34] Yiqing Liang, Numair Khan, Zhengqin Li, Thu Nguyen-Phuoc, Douglas Lanman, James Tompkin, and Lei Xiao. GauFRe: Gaussian deformation fields for real-time dynamic novel view synthesis. *arXiv.cs*, abs/2312.11458, 2023.

[35] Haotong Lin, Sida Peng, Zhen Xu, Tao Xie, Xingyi He, Hujun Bao, and Xiaowei Zhou. Im4d: High-fidelity and real-time novel view synthesis for dynamic scenes. In *Proc. SIGGRAPH Asia*, 2023.

[36] Youtian Lin, Zuozhuo Dai, Siyu Zhu, and Yao Yao. Gaussian-flow: 4d reconstruction with dynamic 3d gaussian particle. In *Proc. CVPR*, 2024.

[37] Huan Ling, Seung Wook Kim, Antonio Torralba, Sanja Fidler, and Karsten Kreis. Align your gaussians: Text-to-4d with dynamic 3d gaussians and composed diffusion models. In *Proc. CVPR*, 2024.

[38] Isabella Liu, Hao Su, and Xiaolong Wang. Dynamic gaussians mesh: Consistent mesh reconstruction from monocular videos. *arXiv*, 2404.12379, 2024.

[39] Lingjie Liu, Weipeng Xu, Marc Habermann, Michael Zollhöfer, Florian Bernard, Hyeongwoo Kim, Wenping Wang, and Christian Theobalt. Neural human video rendering: Joint learning of dynamic textures and rendering-to-video translation. *arXiv.cs*, abs/2001.04947, 2020.

[40] Stephen Lombardi, Tomas Simon, Jason M. Saragih, Gabriel Schwartz, Andreas M. Lehrmann, and Yaser Sheikh. Neural volumes: learning dynamic renderable volumes from images. *ACM Trans. Graph.*, 38(4), 2019.

[41] Matthew Loper, Naureen Mahmood, Javier Romero, Gerard Pons-Moll, and Michael J. Black. SMPL: a skinned multi-person linear model. *ACM Trans. on Graphics (TOG)*, 2015.

[42] Ben Mildenhall, Pratul P. Srinivasan, Matthew Tancik, Jonathan T. Barron, Ravi Ramamoorthi, and Ren Ng. NeRF: Representing scenes as neural radiance fields for view synthesis. In *Proc. ECCV*, 2020.

[43] Richard A. Newcombe, Dieter Fox, and Steven M. Seitz. DynamicFusion: Reconstruction and tracking of non-rigid scenes in real-time. In *Proc. CVPR*, 2015.

[44] David Novotný, Diane Larlus, and Andrea Vedaldi. Capturing the geometry of object categories from video supervision. 2018.

[45] Maxime Oquab, Timothée Darcet, Théo Moutakanni, Huy V. Vo, Marc Szafraniec, Vasil Khalidov, Pierre Fernandez, Daniel HAZIZA, Francisco Massa, Alaaeldin El-Nouby, Mido Assran, Nicolas Ballas, Wojciech Galuba, Russell Howes, Po-Yao Huang, Shang-Wen Li, Ishan Misra, Michael Rabbat, Vasu Sharma, Gabriel Synnaeve, Hu Xu, Herve Jegou, Julien Mairal, Patrick Labatut, Armand Joulin, and Piotr Bojanowski. DINoV2: Learning robust visual features without supervision. *Transactions on Machine Learning Research*, 2024.

[46] Sida Peng, Yuanqing Zhang, Yinghao Xu, Qianqian Wang, Qing Shuai, Hujun Bao, and Xiaowei Zhou. Neural body: Implicit neural representations with structured latent codes for novel view synthesis of dynamic humans. In *Proc. CVPR*, 2021.

[47] Albert Pumarola, Enric Corona, Gerard Pons-Moll, and Francesc Moreno-Noguer. D-NeRF: Neural radiance fields for dynamic scenes. In *Proc. CVPR*, 2021.

[48] Jiawei Ren, Kevin Xie, Ashkan Mirzaei, Hanxue Liang, Xiaohui Zeng, Karsten Kreis, Ziwei Liu, Antonio Torralba, Sanja Fidler, Seung Wook Kim, and Huan Ling. L4GM: Large 4D Gaussian reconstruction model. *arXiv*, 2406.10324, 2024.

[49] Robin Rombach, Andreas Blattmann, Dominik Lorenz, Patrick Esser, and Björn Ommer. High-resolution image synthesis with latent diffusion models. In *Proc. CVPR*, 2022.

[50] Nadine Rüegg, Silvia Zuffi, Konrad Schindler, and Michael J Black. Barc: Learning to regress 3d dog shape from images by exploiting breed information. In *Proc. CVPR*, 2022.

[51] Chris Russell, Rui Yu, and Lourdes Agapito. Video pop-up: Monocular 3D reconstruction of dynamic scenes. In *Proc. ECCV*, 2014.

[52] Prafull Sharma, Ayush Tewari, Yilun Du, Sergey Zakharov, Rares Ambrus, Adrien Gaidon, William T. Freeman, Frédéric Durand, Joshua B. Tenenbaum, and Vincent Sitzmann. Seeing 3d objects in a single image via self-supervised static-dynamic disentanglement. *arXiv.cs*, abs/2207.11232, 2022.

[53] Shuai Shen, Wanhua Li, Zheng Zhu, Yueqi Duan, Jie Zhou, and Jiwen Lu. Learning dynamic facial radiance fields for few-shot talking head synthesis. In *Proc. ECCV*, 2022.

[54] Liangchen Song, Anpei Chen, Zhong Li, Zhang Chen, Lele Chen, Junsong Yuan, Yi Xu, and Andreas Geiger. NeRF-Player: A streamable dynamic scene representation with decomposed neural radiance fields. *IEEE Trans. on Visualization and Computer Graphics*, 29(5), 2023.

[55] Yang Song, Jascha Sohl-Dickstein, Diederik P. Kingma, Abhishek Kumar, Stefano Ermon, and Ben Poole. Score-based generative modeling through stochastic differential equations. In *Proc. ICLR*, 2021.

[56] Colton Stearns, Adam Harley, Mikaela Uy, Florian Dubost, Federico Tombari, Gordon Wetzstein, and Leonidas Guibas. Dynamic Gaussian marbles for novel view synthesis of casual monocular videos. *arXiv*, 2406.18717, 2024.

[57] James Thewlis, Hakan Bilen, and Andrea Vedaldi. Unsupervised learning of object frames by dense equivariant image labelling. In *Proc. NeurIPS*, 2017.

[58] James Thewlis, Hakan Bilen, and Andrea Vedaldi. Unsupervised learning of object landmarks by factorized spatial embeddings. In *Proc. ICCV*, 2017.

[59] James Thewlis, Hakan Bilen, and Andrea Vedaldi. Modelling and unsupervised learning of symmetric deformable object categories. In *Proc. NeurIPS*, 2018.

[60] He Wang, Srinath Sridhar, Jingwei Huang, Julien Valentin, Shuran Song, and Leonidas J. Guibas. Normalized object coordinate space for category-level 6d object pose and size estimation. In *Proc. CVPR*, pages 2642–2651, 2019.

[61] Hengyi Wang, Jingwen Wang, and Lourdes Agapito. Morpheus: Neural dynamic 360° surface reconstruction from monocular RGB-D video. *arXiv.cs*, abs/2312.00778, 2023.

[62] Jianyuan Wang, Christian Rupprecht, and David Novotny. PoseDiffusion: solving pose estimation via diffusion-aided bundle adjustment. In *Proc. ICCV*, 2023.

[63] Jianyuan Wang, Nikita Karaev, Christian Rupprecht, and David Novotny. VGGsFm: visual geometry grounded deep structure from motion. In *Proc. CVPR*, 2024.

[64] Liao Wang, Jiakai Zhang, Xinhang Liu, Fuqiang Zhao, Yanshun Zhang, Yingliang Zhang, Minye Wu, Jingyi Yu, and Lan Xu. Fourier PlenOctrees for dynamic radiance field rendering in real-time. In *Proc. CVPR*, 2022.

[65] Qianqian Wang, Vickie Ye, Hang Gao, Jake Austin, Zhengqi Li, and Angjoo Kanazawa. Shape of motion: 4D reconstruction from a single video. *arXiv*, 2407.13764, 2024.

[66] Shuzhe Wang, Vincent Leroy, Yohann Cabon, Boris Chidlovskii, and Jerome Revaud. DUSt3R: Geometric 3D vision made easy. In *Proc. CVPR*, 2024.

[67] Felix Wimbauer, Nan Yang, Lukas von Stumberg, Niclas Zeller, and Daniel Cremers. MonoRec: Semi-supervised dense reconstruction in dynamic environments from a single moving camera. In *Proc. CVPR*, 2021.

[68] Guanjun Wu, Taoran Yi, Jiemin Fang, Lingxi Xie, Xiaopeng Zhang, Wei Wei, Wenyu Liu, Qi Tian, and Xinggang Wang. 4D gaussian splatting for real-time dynamic scene rendering. In *Proc. CVPR*, 2023.

[69] Shangzhe Wu, Christian Rupprecht, and Andrea Vedaldi. Unsupervised learning of probably symmetric deformable 3D objects from images in the wild. In *Proc. CVPR*, 2020.

[70] Shangzhe Wu, Ruining Li, Tomas Jakab, Christian Rupprecht, and Andrea Vedaldi. Magicpony: Learning articulated 3d animals in the wild. *arXiv.cs*, 2022.

[71] Shangzhe Wu, Tomas Jakab, Christian Rupprecht, and Andrea Vedaldi. DOVE: Learning deformable 3D objects by watching videos. In *IJCV*, 2023.

[72] Shangzhe Wu, Ruining Li, Tomas Jakab, Christian Rupprecht, and Andrea Vedaldi. MagicPony: Learning articulated 3D animals in the wild. In *Proc. CVPR*, 2023.

[73] Jianfeng Xiang, Zelong Lv, Sicheng Xu, Yu Deng, Ruicheng Wang, Bowen Zhang, Dong Chen, Xin Tong, and Jiaolong Yang. Structured 3D latents for scalable and versatile 3D generation. *arXiv*, 2412.01506, 2024.

[74] Tianyi Xie, Zeshun Zong, Yuxing Qiu, Xuan Li, Yutao Feng, Yin Yang, and Chenfanfu Jiang. PhysGaussian: Physics-integrated 3D Gaussians for generative dynamics. *arXiv.cs*, abs/2311.12198, 2023.

[75] Yunzhi Yan, Haotong Lin, Chenxu Zhou, Weijie Wang, Haiyang Sun, Kun Zhan, and Xianpeng Lang. Street gaussians for modeling dynamic urban scenes. *arXiv*, 2024.

[76] Gengshan Yang, Deqing Sun2, Varun Jampani, Daniel Vlasic, Forrester Cole, Huiwen Chang, Deva Ramanan, William T. Freeman, and Ce Liu. LASR: Learning articulated shape reconstruction from a monocular video. In *Proc. CVPR*, 2021.

[77] Gengshan Yang, Minh Vo, Natalia Neverova, Deva Ramanan, Andrea Vedaldi, and Hanbyul Joo. BANMo: Building animatable 3d neural models from many casual videos. In *Proc. CVPR*, 2022.

[78] Gengshan Yang, Chaoyang Wang, N. Dinesh Reddy, and Deva Ramanan. Reconstructing animatable categories from videos. In *Proc. CVPR*, 2023.

[79] Lihe Yang, Bingyi Kang, Zilong Huang, Zhen Zhao, Xiaogang Xu, Jiashi Feng, and Hengshuang Zhao. Depth anything V2. *arXiv*, 2406.09414, 2024.

[80] Zeyu Yang, Hongye Yang, Zijie Pan, and Li Zhang. Real-time photorealistic dynamic scene representation and rendering with 4d gaussian splatting. In *Proc. ICLR*, 2024.

[81] Chun-Han Yao, Wei-Chih Hung, Yuanzhen Li, Michael Rubinstein, Ming-Hsuan Yang, and Varun Jampani. LASSIE: learning articulated shapes from sparse image ensemble via 3d part discovery. *arXiv.cs*, abs/2207.03434, 2022.

[82] Chun-Han Yao, Amit Raj, Wei-Chih Hung, Yuanzhen Li, Michael Rubinstein, Ming-Hsuan Yang, and Varun Jampani. ARTIC3D: Learning robust articulated 3D shapes from noisy web image collections. *Proc. NeurIPS*, 2023.

[83] Yuyang Yin1, Dejia Xu2, Zhangyang Wang, Yao Zhao, and Yunchao Wei. 4DGen: Grounded 4D content generation with spatial-temporal consistency. *arXiv.cs*, 2023.

[84] Jae Shin Yoon, Kihwan Kim, Orazio Gallo, Hyun Soo Park, and Jan Kautz. Novel view synthesis of dynamic scenes with globally coherent depths from a monocular camera. In *Proc. CVPR*, 2020.

[85] Daiwei Zhang, Gengyan Li, Jiajie Li, Mickaël Bressieux, Otmar Hilliges, Marc Pollefeys, Luc Van Gool, and Xi Wang. EgoGaussian: Dynamic scene understanding from egocentric video with 3D gaussian splatting. *arXiv.cs*, abs/2406.19811, 2024.

[86] Junyi Zhang, Charles Herrmann, Junhwa Hur, Luisa Polania Cabrera, Varun Jampani, Deqing Sun, and Ming-Hsuan Yang. A tale of two features: Stable diffusion complements DINO for zero-shot semantic correspondence. *arXiv.cs*, abs/2305.15347, 2023.

[87] Junyi Zhang, Charles Herrmann, Junhwa Hur, Varun Jampani, Trevor Darrell, Forrester Cole, Deqing Sun, and Ming-Hsuan Yang. MonST3R: a simple approach for estimating geometry in the presence of motion. *arXiv*, 2410.03825, 2024.

[88] Yuyang Zhao, Zhiwen Yan, Enze Xie, Lanqing Hong, Zhen-guo Li, and Gim Hee Lee. Animate124: Animating one image to 4D dynamic scene. *arXiv.cs*, abs/2311.14603, 2023.

[89] Silvia Zuffi, Angjoo Kanazawa, David W. Jacobs, and Michael J. Black. 3D menagerie: Modeling the 3D shape and pose of animals. In *Proc. CVPR*, 2017.

[90] Silvia Zuffi, Angjoo Kanazawa, and Michael J Black. Lions and tigers and bears: Capturing non-rigid, 3d, articulated shape from images. In *Proc. CVPR*, 2018.

[91] Silvia Zuffi, Ylva Mellbin, Ci Li, Markus Hoeschle, Hedvig Kjellström, Senya Polikovsky, Elin Hernlund, and Michael J Black. Varen: Very accurate and realistic equine network. In *Proc. CVPR*, pages 5374–5383, 2024.

Appendix

A. Generalization to unseen categories

Given the generalization capabilities of our method demonstrated within a single category, we analyze the generalization of a model trained on a single category to unseen categories. Specifically, we consider a model trained on horses and evaluate its performance on cow and sheep categories. We evaluate our approach using the same datasets as for the horses, PASCAL VOC [12] and Animodel [18], following the same evaluation protocol, with results reported in Tab. A3. Furthermore, we provide additional qualitative results on the same dataset in Fig. A8. Our method exhibits strong zero-shot generalization to these categories, outperforming state-of-the-art approaches on both datasets, despite being trained exclusively on a single horse model.



Figure A8. **Results on unseen categories.** A version of our model trained only on the horse category also demonstrates robust generalization to the unseen categories such as cow and sheep, despite being trained solely with a single horse model.

B. Limitations

Despite demonstrating surprising generalization, a current limitation of our method is that any additional synthetic 3D models added to the training dataset would have to be in the same canonical space as the training data. Addressing the challenging problem of aligning the canonical spaces of multiple 3D models would allow us to train on significantly larger datasets which could in turn lead to significant gains in performance for our proposed model. Another limitation of our method is that it is not specifically trained to handle occlusions caused by other objects. This is a limitation shared with other methods, such as 3D-Fauna [33, 72]. To address this, we plan to extend the data generation pipeline to include synthetic occlusions. Additionally, as the 3D reconstruction problem is often ambiguous for the unseen parts of objects, our method predicts only the expectation over all possible reconstructions, which can lead to unrealistic results for the invisible regions. We illustrate our typical failure cases in Fig. A9.

C. Technical details

Network architecture. We obtain the segmentation mask M using the Segment Anything method [23]. The feature extractor Ψ is based on [86] which combines pre-trained DINOv2 [45] and StableDiffusion [49] networks. Training image features are reduced to a 64-dimensional space using

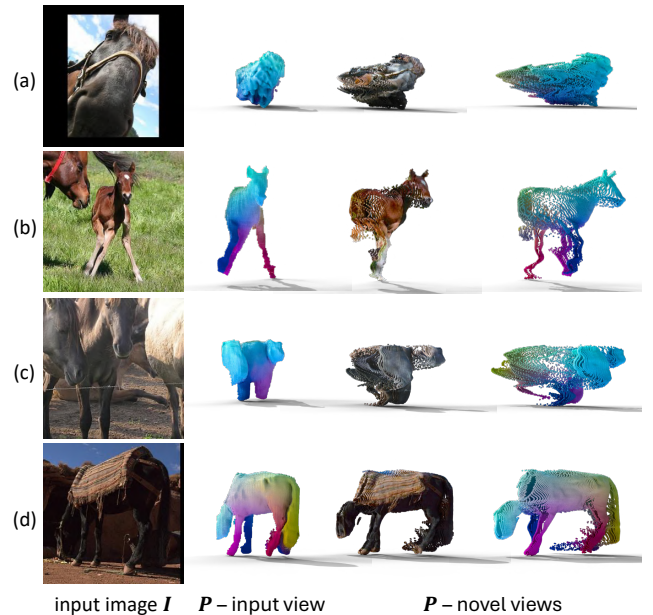


Figure A9. **Typical failure cases.** We illustrate representative failure cases caused by (a) extreme viewpoints, (b) shapes and poses far from the training distribution, and (c-d) inaccuracies in the object segmentation masks.

Method	PCK (%)				Chamfer Distance (cm)			
	Cow Sheep		Real-Sized		Normalized			
	Cow	Sheep	Cow	Sheep	Cow	Sheep		
A-CSM [26]	26.3	28.6	6.71 \pm 1.81	2.84 \pm 0.77	2.35 \pm 0.68	2.48 \pm 0.70		
MagicPony [72]	42.5	41.2	7.22 \pm 1.53	3.43 \pm 0.73	2.53 \pm 0.59	3.00 \pm 0.68		
Farm3D [18]	40.2	36.1	6.91 \pm 1.49	3.79 \pm 0.55	2.41 \pm 0.54	3.31 \pm 0.49		
3D-Fauna [33]	—	—	9.19 \pm 2.40	3.51 \pm 0.88	3.20 \pm 0.80	3.06 \pm 0.76		
Ours	63.0	64.2	4.74 \pm 1.40	2.32 \pm 0.78	1.67 \pm 0.55	2.03 \pm 0.71		

Table A3. **Evaluation on unseen cow and sheep categories.** We evaluate on PASCAL VOS, reporting PCK@0.1 (higher is better \uparrow), and on Animodel [18], reporting the bi-directional Chamfer Distance in centimeters (lower is better \downarrow). Our model, trained solely on data from a single horse model, outperforms state-of-the-art approaches, which were trained on data that included these specific categories.

PCA following [70]. The dual point map predictors Φ_Q and Φ_P leverage a convolutional U-Net architecture based on [55], comprising two blocks each and trained from scratch. We predict $N = 4$ layers for layered amodal point maps as more have little effect on the performance (Sec. 4.4), likely due to the low frequency of multiple self-occlusions in our datasets. The number of layers can be easily increased should the data require it. The output resolution of the layered point maps is set to 160×160 .

Training. We use the Adam optimizer [22] for training. Our model is trained for 100k steps with a batch size of 12. The learning rate is set to 6×10^{-4} , with a step scheduler applied, featuring a 30k-step period and a decay factor of 0.5.

Training dataset. The training dataset consists of approximately 30k rendered images per category. We generate these images using a single rigged model per animal species. For cow, sheep, and goat, we use a separate model for each sex category, incorporating major sex-specific attributes such as horns. Each model includes up to three different textures and 50 animated actions, such as running, walking, and drinking. We also randomly sample from a pool of 742 HDRI environmental maps to provide diverse lighting conditions for the training images. We then randomly sample camera viewpoints and poses from the animated actions to generate the training images. Fig. 4 showcases the horse model and some of the generated images used for training.

D. Benchmark details

We introduce **Animodel-Points**, a benchmark specifically designed to address the limitations of using the original Animodel benchmark for evaluating point cloud generation models. Previous evaluations on Animodel were suboptimal for two primary reasons: the benchmark was designed for **meshes**, not point clouds, and its evaluation backend (`trimesh.registration`)² only optimizes a one-sided

²Trimesh: A Python library for loading and using triangular meshes. <https://github.com/mikedh/trimesh>

Chamfer distance.

Animodel-Points resolves these issues by establishing a new protocol that directly evaluates point clouds using a more robust metric. The key improvements are:

- **Model-view coordinates:** Targets are defined in model-view coordinates up to a depth offset, which allows for the additional evaluation of camera alignment performance.
- **Bidirectional Chamfer distance:** The evaluation protocol minimizes the mean squared bidirectional Chamfer distance, aligning the optimization objective with the reported cost for a fairer assessment.
- **Standardized point cloud processing:** A clear pre-processing and evaluation pipeline ensures consistency and comparability of results.

Methodology

The methodology is divided into two stages: preparing the ground truth data and the protocol for evaluating a prediction.

Data pre-processing To convert the original Animodel meshes into the Animodel-Points format, we apply the following steps:

1. **Coordinate transformation:** The source mesh is transformed into model-view coordinates.
2. **Uniform scaling:** The mesh is uniformly scaled by a factor of $V^{-1/3}$, where V is the mesh volume, to normalize its size.
3. **Point sampling:** 20,000 points are uniformly sampled from the surface of the scaled mesh to serve as the ground truth target.

Evaluation protocol For a given generated point cloud, the following evaluation steps are performed:

1. **Resampling:** If the input point cloud does not contain 20,000 points, it is resampled to this size.
2. **Rotational ambiguity handling:** The 20,000 point sample is duplicated, and the duplicate is rotated 180 degrees around its vertical axis.
3. **Subsampling for fitting:** A subset of 10,000 points is sampled from the input to be used in the alignment pro-

Method	Chamfer Distance (cm)					
	Real-Sized			Normalized		
	Horse	Cow	Sheep	Horse	Cow	Sheep
A-CSM [26]	7.60 \pm 3.07	6.71 \pm 1.81	2.84 \pm 0.77	2.73 \pm 1.13	2.35 \pm 0.68	2.48 \pm 0.70
MagicPony [72]	7.19 \pm 2.35	7.22 \pm 1.53	3.43 \pm 0.73	2.58 \pm 0.80	2.53 \pm 0.59	3.00 \pm 0.68
Farm3D [18]	7.65 \pm 2.21	6.91 \pm 1.49	3.79 \pm 0.55	2.76 \pm 0.83	2.41 \pm 0.54	3.31 \pm 0.49
3D-Fauna [33]	8.69 \pm 2.38	9.19 \pm 2.40	3.51 \pm 0.88	3.13 \pm 0.85	3.20 \pm 0.80	3.06 \pm 0.76
Trellis [73]	5.11 \pm 3.53	5.50 \pm 3.37	2.23 \pm 1.39	1.85 \pm 1.31	1.93 \pm 1.23	1.96 \pm 1.22
Ours	3.13 \pm 2.13	2.63 \pm 1.23	1.52 \pm 0.88	1.11 \pm 0.73	0.92 \pm 0.43	1.33 \pm 0.78

Table A4. **Evaluation on Animodel.** We evaluate on Animodel [18], reporting the bi-directional Chamfer Distance in centimeters (lower is better \downarrow). Ours include results from models trained on data from each category.

cess.

4. **Alignment:** Both the original and rotated samples are aligned to the ground truth target using the Iterative Closest Point (ICP) algorithm. The process runs for a maximum of 200 steps or until convergence, using the MSE bidirectional Chamfer distance as the objective function.
5. **Final score:** The lower of the two costs from the alignment steps is reported as the final score.

Chamfer distance performance is evaluated by providing scale, rotation, and translation degrees of freedom to the transformation estimation. Model-view chamfer distance is evaluated by restricting the degrees of freedom to just scale and translation.

Published results Previously published results were reported on the Animodel benchmark and are available in this table Tab. A4.